VTT Technical Research Centre of Finland

DTRC Propeller 4119 calculations at VTT

Sanchez Caja, Antonio

Published in:
Proceedings of the 22nd ITTC Propulsion Committee Propeller RANS/Panel Method Workshop

Published: 01/04/1998

Document Version
Publisher's final version

P4119 RANS Calculations at VTT

by

Antonio Sánchez-Caja

VTT Manufacturing Technology, Maritime and Mechanical Engineering

1 INTRODUCTION

Calculations of viscous flow around DTRC propeller 4119 were made at VTT in 1996 and reported in Sánchez-Caja (1996). The results presented here are based on the data files of such calculations. The FINFLO RANS code was used in this work. The development of the FINFLO RANS (=Reynolds-Averaged-Navier-Stokes) code was started at the Department of Aerodynamics of Helsinki University of Technology (=HUT) and has been continued at the Departments of Aerodynamics and Applied Thermodynamics of HUT. Presently VTT Manufacturing Technology is working together with HUT to apply and extend the FINFLO code to the analysis of rotating fluid machinery and free surface flow around ship hulls. These two projects form parts of the Finnish National CFD Technology Research Programme which is funded by TEKES (Technology Development Centre of Finland) and VTT. Pylkkänen and co-authors (1997) have reported on the contribution of VTT to this co-operative work.

In Section 2 of this paper the numerical method is briefly described (Sánchez-Caja, 1996; Pylkkänen et al., 1997). Section 3 gives details of the propeller grid and input parameters used in the calculations. Sections 4 provides the validation results for propeller 4119. The calculated data are compared with the measurements of Jessup (1989).

2 NUMERICAL METHOD

2.1 Governing Equations

The flow simulation is based on the solution of Reynolds-averaged Navier-Stokes equations together with the equations for the turbulent kinetic energy k and dissipation of turbulence ε. They can be written in the following form

$$\frac{\partial U}{\partial t}+\frac{\partial (F-F_v)}{\partial x}+\frac{\partial (G-G_v)}{\partial y}+\frac{\partial (H-H_v)}{\partial z}=Q \qquad (1)$$

where U is $(\rho, \rho u, \rho v, \rho w, E, \rho k, r\varepsilon)^T$; F, G and H are the inviscid fluxes; F_v, G_v and H_v are the viscous fluxes; u, v and w are the absolute velocity components; ρ is the density and E is the total internal energy. The source term Q has non-zero components only for the turbulence equations. For propeller analysis, the equations are solved in a coordinate system which rotates around the x-axis with an angular velocity Ω. In this case Q has the additional component $(0, 0, \rho\Omega w, -\rho\Omega v, 0, 0, 0)$. More information can be found in Siikonen & Pan (1992) and Pitkänen & Siikonen (1995).

FINFLO has the possibility to use different turbulent models (Rautaheimo & Siikonen, 1995; Siikonen, 1994): algebraic turbulence models (Baldwin-Lomax, Cebeci-Smith), the low-Reynolds' number k-ε model proposed by Chien, the explicit Reynolds-stress model of Speziale et al. and the Reynolds-stress model of Shima.

The concept of artificial compressibility can also be used in FINFLO to seek the solution of the equations for incompressible flows. The continuity equation is then modified by adding an artificial time derivative of pressure and an artificial speed of sound. The system of equations becomes hyperbolic and consequently has similar properties to those of compressible flows.

2.2 Discretization

A finite-volume technique is used for solving the equations. The differential equations are integrated over a computational cell

$$V_i \frac{dU_i}{dt} = \sum_{faces} -S.F^* + V_i Q_i \qquad (2)$$

where

$$F^* = n_x(F-F_v) + n_y(G-G_v) + n_z(H-H_v) \qquad (3)$$

and the summation is extended over the faces of the computational cell. In a rotating frame, i. e. for propeller calculations, the functional form of the flux equations is similar to the case without rotation. The difference is that in a rotating frame the motion of the cell faces is taken into account in the evaluation of energy flux and convective velocities.

Roe's method is applied for the evaluation of the inviscid fluxes. The flux is calculated with the help of a rotation matrix which transforms the dependent variables to a local system of coordinates normal to the cell surface (Siikonen, 1994). The interface values are evaluated by a MUSCL-type formula.

2.3 Solution Algorithm

The discretized equations are integrated in time by applying the DDADI-factorization. This is based on the splitting of the Jacobians of the flux terms. The resulting approximately factored implicit scheme consists of a backward and a forward sweep in every coordinate direction. The sweeps are based on a first-order upwind differencing. In order to accelerate convergence, local time stepping and a multigrid method are also implemented in FINFLO (Siikonen et al., 1990).

More detailed descriptions of FINFLO can be found in the references of this paper (Siikonen et al. 1990; Lehtimäki et al., 1996).

3 CALCULATIONS

3.1 Grid and Boundary Conditions

The geometry of the computational grid for propellers is obtained using a commercial grid generator program. An auxiliary program has been developed to provide the input propeller geometry to the grid generator program (Sánchez-Caja,1996).

The space between two contiguous propeller blades is modeled to take full advantage of the symmetry of homogeneous flow and geometry. The grid consists of six blocks. Groups of two blocks representing the space near and far away from the hub are located upstream, downstream and in-between the propeller blades. The space near the hub extends from hub to the propeller radius. The space further away from the hub extends from the propeller radius to the outermost external boundary.

Fine grid spacings are used in the vicinity of the leading and trailing edges of the propeller blades in the chordwise direction and near the blade tip and hub in the radial direction. The minimum grid spacing in the circumferential direction for the resolution of the boundary layer was 0.000002.

The dimensions of the blocks closer to the hub in the *I, J* and *K* directions were 48*72*80, 64*72*80 and 56*72*80 for the blocks located upstream, downstream and in-between the propeller blades, respectively. *I* stands for the axial direction, *J* for the circumferential direction, and *K* for the radial direction. The remaining three blocks have the same dimensions except for the maximum *K* index that was 32. The total number of cells was 1354752. This grid is finally supplied with two additional blocks to enforce the boundary conditions at the outlet.

The dimensions of the second level grid are 24*36*40, 32*36*40 and 28*36*40 for the three blocks. Figure 1 depicts the second grid level for propeller 4119.

The hub and blade surfaces of propeller are rotating solid walls. The lateral surfaces adjacent to the propeller blades have a periodic boundary condition. Block boundaries, where two adjacent block surfaces are coincident, are defined as connectivities. Uniform flow conditions are applied for the inlet and external boundary surfaces, and the streamwise gradients of the velocities are set to zero on the outlet surface.

3.2 Calculations

The uniform inflow calculations were made for the 0.305 m diameter model propeller rotating at 10 rps. The inflow speeds were adjusted to correspond the advance numbers of J=0.3, 0.5, 0.833, and 1.1. For J=0.833 the uniform inflow speed was 2.54 m/s.

Since the incompressible version of FINFLO was not available when the present work was initiated, the propeller operating conditions were scaled to simulate operation at constant Reynolds number in compressible flow. The fluid was air. Assuming that the Mach number based on the rotational speed is not higher than 0.25 the scale factor for the propeller geometry was 1.437. The inflow velocity was set to 22.55 m/s and the rotational speed, to 61.8 rps.

The k-ε turbulence model has been used in the present calculations (Siikonen, 1994). The Baldwin-Lomax turbulence model was found to overpredict the thrust and torque.

In 1996 the FINFLO version with pseudo-compressibility became available. The compressible code was used in all the calculations because the compressible flow calculations converged faster. The performance predictions of the calculations were not much affected by the FINFLO version used. Table 1 gives the turbulence parameters used in the P4119 calculations.

Minimum turbulence level	0.001
Minimum dissipation of kinetic energy	0.01
Maximum non-dimensional turbulence coefficient	5000
Free-stream and initial turbulence level (Tu)	0.05
Free-stream and initial non-dimensional turbulence coeff.	10

Table 1. Turbulence parameters for P4119.

The convergence history of the norm of the overall drag coefficient is shown in Figure 2 for the first grid level. Figures 3 and 4 illustrate the convergence histories of the norm of k and ε residual for the first grid level. The Courant numbers were 2.5 for the second grid level and for the 500 first iterations of the first grid level. From the 500^{th} iteration the Courant number was set to 0.5. The multigrid level was two. The change of Courant number was due to instabilities in the convergence history for the tip region of the dowstream block. Later it has been found that an alternative solution for this problem is to reduce multigrid level from two to one in this area without reducing the Courant number.

At low advance numbers (J=0.3-0.5) the multigrid level was fixed to one for the calculation with the finest grid in order to improve convergence. At the highest advance number (J=1.1) the multigrid level was two.

The non-dimensional sublayer-scaled distance from the surface y^+ was lower than 2 along most of the chord at 0.7 non-dimensional radius.

The CPU time per iteration in the second grid level using a SGI R8000 processor system was about 19 seconds for one multigrid level and about 32 seconds for two multigrid levels using a single processor. These numbers have to be multiplied by 8 to get the corresponding values for the finest grid level calculations. The block dimensions were chosen to easily distribute the load between three processors for parallel computation.

4 CFD RESULTS FOR P4119

4.1 Open Water Performance

Table 2 gives the calculated performance for advance numbers ranging from 0.3 to 1.1 (Sánchez-Caja, 1996). The second level calculations yield clearly more inaccurate performance predictions.

The predictions of thrust and torque are accurate for the design advance number. Differences lower than 1.5 percent are found. The corresponding efficiency is calculated with an error rate lower than 3 percent. At low advance ratios, i.e. J=0.3-0.5, the differences from the experimental values are greater for the thrust and torque coefficients, however the efficiency is predicted with reasonable accuracy. At the highest validation advance number the open water efficiency curve has a very steep slope, which magnifies small errors. For these advance ratios the computations were found to converge more slowly and were stopped at the 2000^{th} iteration. This point represents the trend in the convergence history of the oscillating overall drag and lift coefficient.

J	0.3	0.5	0.833	1.1
K_T (calculated, 2^{nd} grid level)	0.390	0.289	0.140	0.013
K_T (calculated, 1^{st} grid level)	0.399*	0.294*	0.144	0.0203
K_Q (calculated, 2^{nd} grid level)	0.0629	0.0502	0.0290	0.0112
K_Q (calculated, 1^{st} grid level)	0.0626*	0.0495*	0.0284	0.0107
η_0 (calculated, 2^{nd} grid level)	0.296	0.458	0.638	0.206
η_0 (calculated, 1^{st} grid level)	0.304*	0.473*	0.673	0.331

Table 2. Calculated performance of P4119. The asterisk (*) indicates that the calculations were stopped at the 2000^{th} iteration.

Calculations have been also repeated later for the design advance number using the pseudo-compressibility approach. The performance coefficients were not much affected. Differences less than 1.4 percent were found and the efficiency was practically the same.

Later grid developments for other propellers have shown that redistributing the cells to represent more accurately the propeller leading edge in the outer radii improves the prediction of efficiency to 1-1.5% for the design advance number.

4.2 Calculations Vs. Measurements

Blade Pressure Distribution. The pressure coefficient based on the relative velocity at the 0.7 non-dimensional radius has been calculated in two different ways: using the pressure on the blade surface, $C_P=(p-p_0)/(0.5*\rho*V_R^2)$ and using the LDV approximation, $1-V^2/V_R^2$ at the edge of the blade boundary layer. In these formulae p and p_0 are the pressure at the point of interest and at infinity, respectively; ρ is the density; V is the total velocity, and V_R is the relative inflow at 0.7 nondimensional radius. The results are presented in Figure 5 for the advance number J=0.833. The pressure coefficients of curves 2^{nd} and 4^{th} are based on the LDV approximation. These two curves agree well with measurements (Jessup, 1989; Fig. 3-28b). The curves 1^{st} and 3^{rd} give the pressure coefficients obtained from the calculated pressure on the blade surface. These two methods of obtaining the pressure coefficients result in different data. Viscous effects are responsible for the differences near the trailing edge. However, the differences near the leading edge are probably caused by the difficulty of measuring velocities close to the blade surface (for instance, in our calculation at X/C=0.05 on the suction side V^2/V_R^2-1 reaches a maximum of 0.139 close to the surface but a value of about 0.09 is obtained over a larger area above it.)

Circumferential Field Point Velocities. Figure 6 gives the circumferential field point velocities at the x/R=0.3281 plane and r/R=0.924. Figure 7 shows the velocities at r/R=0.7 on the same plane. The zero angular position of the pictures is not the same as that in Jessup's paper. The agreement with the measurements is very good for r/R=0.7, and moderately good for r/R=0.924 due to a small underprediction of the wake contraction (Jessup, 1989; Figs. 3-50).

Phase Averaged, Time Dependent Field Point Velocities. Figure 8 shows the circumferential field point velocities at the x/R=0.3281 plane. The agreement with the measurements is good especially for the tangential velocity. The axial and radial velocities are a little overpredicted (Jessup, 1989; Figs. 3-12a,b,c).

Blade Boundary Layer. Figure 9 gives the streamwise boundary layer at r/R=0.7 and x/c=0.9 on the blade suction side. Figure 10 shows the corresponding values at r/R=0.7 and x/c=0.95 on the blade pressure side. The agreement with the measurements is good (Jessup, 1989; Figs. 3-30, 4-30).

4.3 Flow Patterns

Figures 11 and 12 from Sánchez-Caja (1996) show the distribution of the static pressure and the limiting streamlines on the suction and pressure sides of the propeller and hub for the advance number of 0.833, respectively. The directions of calculated streamlines are similar to those seen in the paint test results published in the 20th ITTC Propulsor Committee Report (1993, Figs. 2.6 & 2.7). Figure 13 show the streamlines and static pressure contours on the suction side of the blade on the suction side for an advance number of 0.5. The generation of the tip vortex around the propeller leading edge is apparent. At low advance numbers the tip vortex is started on the leading edge at a point upstream the tip, which coincides with experimental observations.

Figures 14 from Sánchez-Caja (1996) presents contours of non-dimensional pitch-line vorticity on a plane located at x/R=0.328. The measured maximum non-dimensional intensity in the center of the tip-vortex core is about 40. The corresponding calculated values are about 28. The location of the tip vortex is close to that observed in experiments given in Figure 3-66b of Jessup (1989). The contraction of the slipstream is somewhat under-predicted.

5 CONCLUSION

The open water flow patterns and performance coefficients for DTRC propeller 4119 have been calculated using the FINFLO code. The predictions of thrust and torque for Propeller 4119 are within 1.5 % of the experimental values for advance numbers close to the design value. The flow patterns are generally well predicted with the k-ε turbulent model. A better prediction of the tip vortex flow requires a more sophisticated turbulence model and a grid adapted to the tip wake.

6 REFERENCES

1993, "20th ITTC Propulsor Committee Report", San Francisco, 19-25 Sept. 1993.

Jessup, S.D., 1989, "An Experimental Investigation of Viscous Aspects of Propeller Blade Flow",Washington DC, The Catholic University of America, PhD Dissertation.

Lehtimäki, R., Laine, S., Siikonen, T., Salminen, E., 1996, "Navier-Stokes Calculations for a Complete Aircraft", 20th ICAS Congress, Sorrento, ICAS-92-4.2.1.

Pitkänen, H., Siikonen, T., 1995, "Simulation of Viscous Flow in a Centrifugal Compressor. Espoo", HUT, Laboratory of Aerodynamics, Report No. B-46.

Pylkkänen, J.V., Sánchez-Caja, A., Sundell, T., 1997, "Application of FINFLO RANS Solver to Naval Hydrodynamics", International CFD Conference, Ulsteinvik, May 97

Rautaheimo, P., Siikonen, T., 1995, "Numerical Methods for Coupling the Reynolds-Averaged Navier-Stokes Equations with the Reynolds-Stress Turbulence Model", Espoo, HUT, Laboratory of Applied Thermodynamics, Report No. 81.

Sánchez-Caja, A., 1996, "Numerical Calculation of Viscous Flow around DTRC Propeller 4119 for Advance Number Range 0.3-1.1 Using FINFLO Navier-Stokes Solver", Espoo, VTT Manufacturing Technology Technical Report VALB141A.

Siikonen, T., 1994, "An Application of Roe´s Flux-Difference Splitting for k-ε Turbulence Model", International Journal for Numerical Methods in Fluids, Vol. 21, No. 11. (Espoo, HUT, Laboratory of Aerodynamics, Report No. A-15.)

Siikonen, T., Hoffren, J., Laine, S., 1990, "A Multigrid LU Factorization Scheme for the Thin-layer Navier-Stokes Equations", 17th ICAS Congress, Stockholm.

Siikonen, T., Pan, H.-C.,1992, "An Application of Roe´s Method for the Simulation of Viscous Flow in Turbomachinery", First European Computational Fluid Dynamics Conference, Brussels, 7-11 Sep 1992.

7 NOTATIONS

c blade section chord length
D propeller diameter
g acceleration due to gravity
J V/(nD), advance coefficient
K_Q $Q/(\rho n^2 D^5)$, torque coefficient
K_T $T/(\rho n^2 D^4)$, thrust coefficient
n rate of rotation
p pressure
p_0 pressure at infinity
Q torque
R propeller radius
r radial coordinate
s coordinate along propeller chord
T thrust
V advance velocity; total velocity at the edge of the blade boundary layer.
V_R resultant inflow speed to the blade section
x coordinate along propeller axis
y^+ non-dimensional sublayer-scaled distance from the surface
η_O propeller open water efficiency
ρ density

APPENDIX

It has been said in Section 4.1 that later grid developments for other propellers have shown that redistributing the cells to represent more accurately the propeller leading edge in the outer radii improves the prediction of efficiency to 1-1.5% for the design advance number and finest grid level. For this reason, recently it was decided to perform a new calculation for propeller DTRC 4119 at J=0.833 using an improved grid and the pseudo-compressibility approach. No scaling of the geometry was needed. Table 3 shows the calculated performance. The prediction of efficiency is noticeably improved for the 2nd grid level and falls within 1.7 percent of the experimental value for the finer grid. It is interesting to note that the grid level seems to affect mainly to the prediction of torque, and that it does not affect that of thrust too much.

J	0.833
K_T (calculated, 2nd grid level)	0.141
K_T (calculated, 1st grid level)	0.143
K_Q (calculated, 2nd grid level)	0.0285
K_Q (calculated, 1st grid level)	0.0278
η_0 (calculated, 2nd grid level)	0.658
η_0 (calculated, 1st grid level)	0.681

Table 3. Performance prediction with the new grid and the pseudo-compressibility approach.

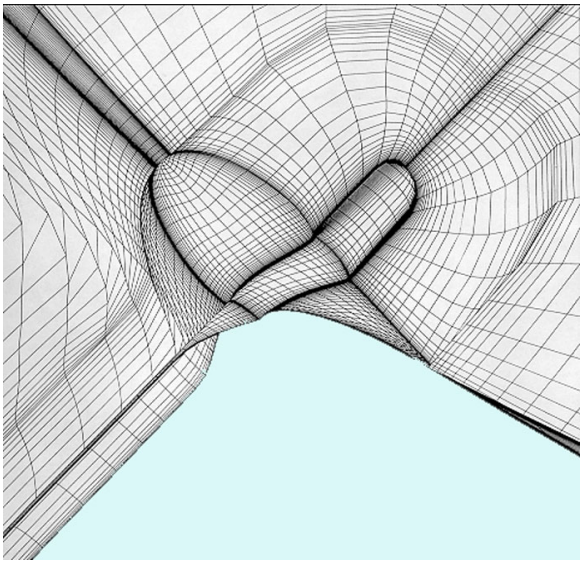

Figure 1. Grid used in the flow predictions.

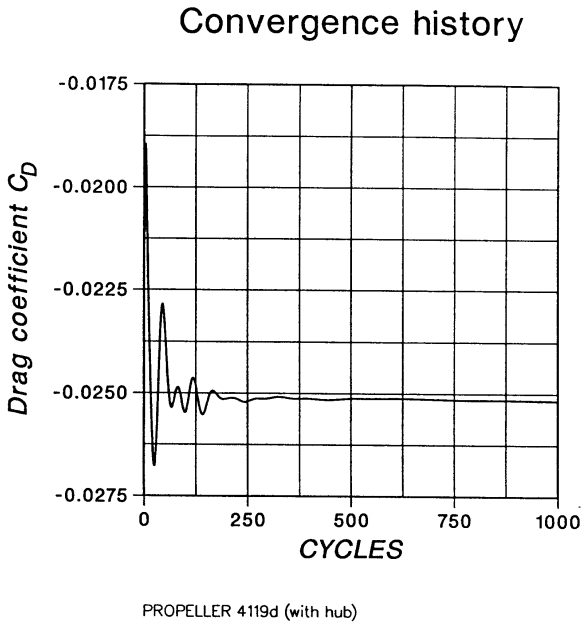

Figure 2. Overall drag coefficient convergence.

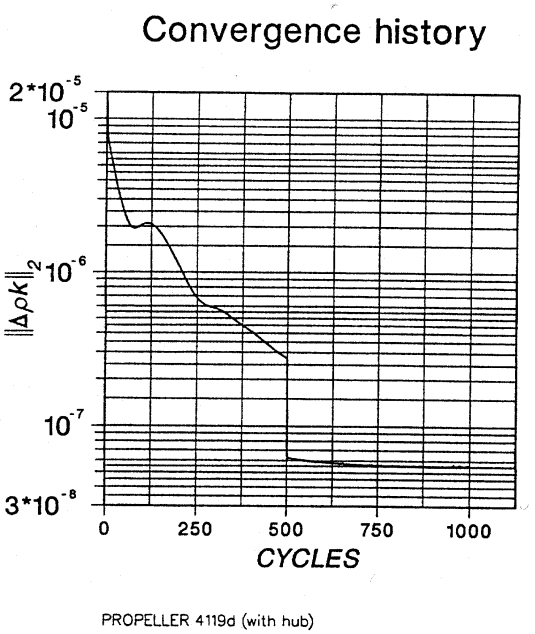

Figure 3. Convergence history of the norm of the k residual for the first grid level (J=0.833).

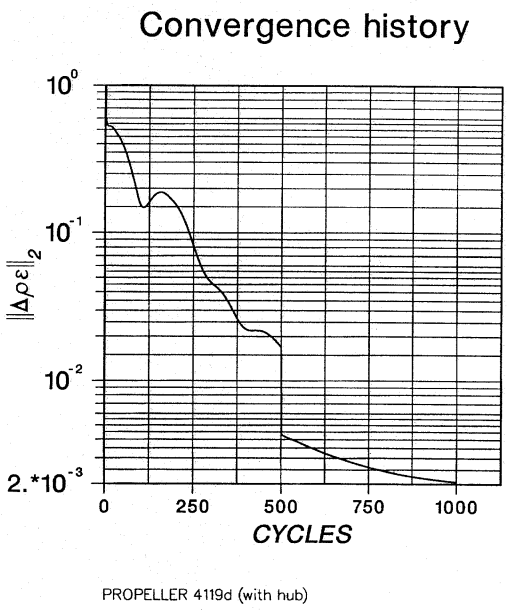

Figure 4. Convergence history of the norm of the ε residual for the first grid level (J=0.833).

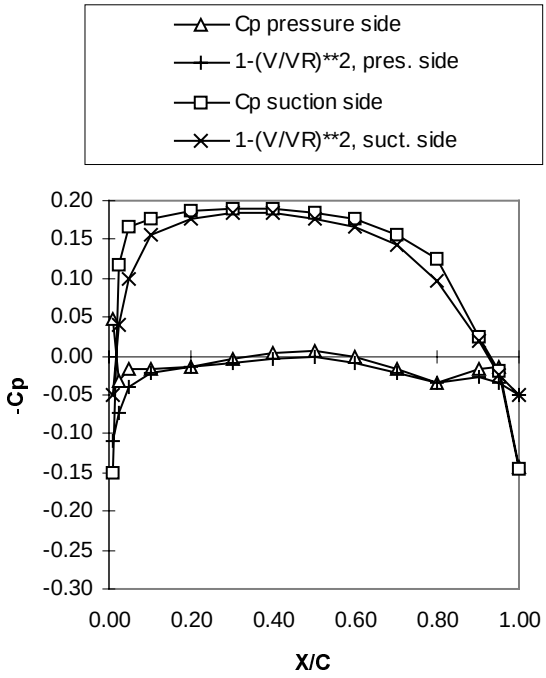

Figure 5. Chordwise distribution of -Cp based on the relative velocity at r/R=0.7.

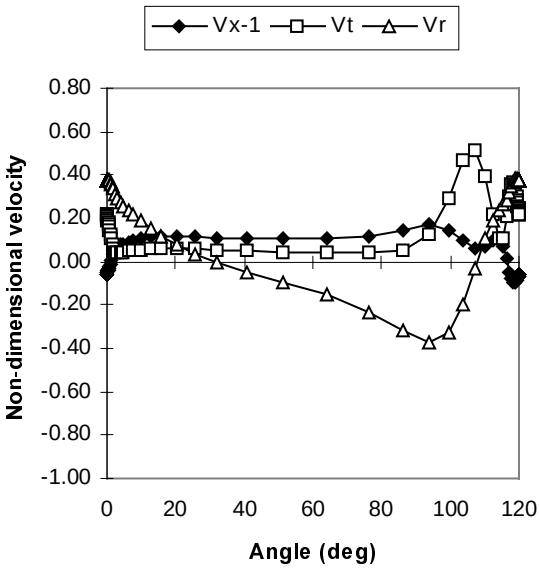

Figure 6. Angular distribution of dimensionless velocities at x/R=0.3281 and r/R=0.924.

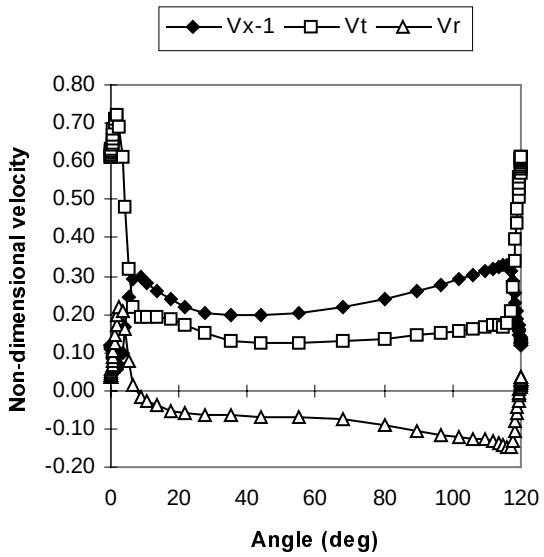

Figure 7. Angular distribution of dimensionless velocities at x/R=0.3281 and r/R=0.70.

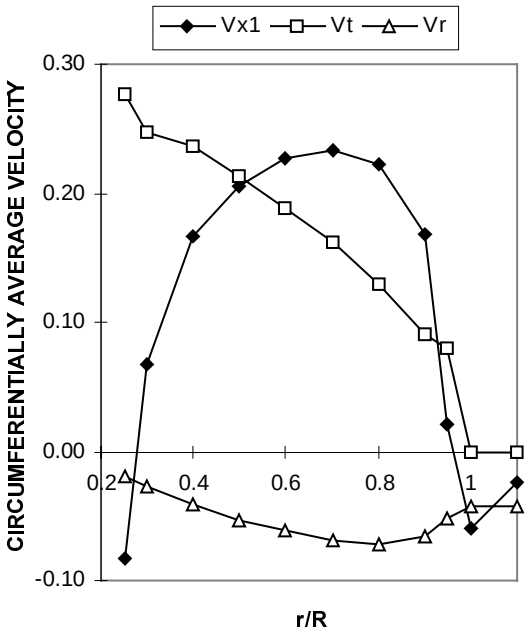

Figure 8. Radial distribution of circumferentially-average dimensionless velocities at x/R=0.3281.

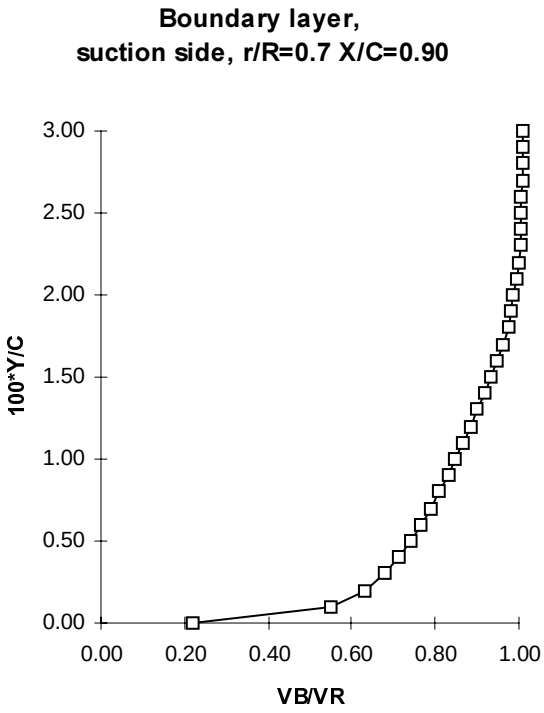

Figure 9. Boundary layer at r/R=0.7 and x/c=0.9 on the blade suction side.

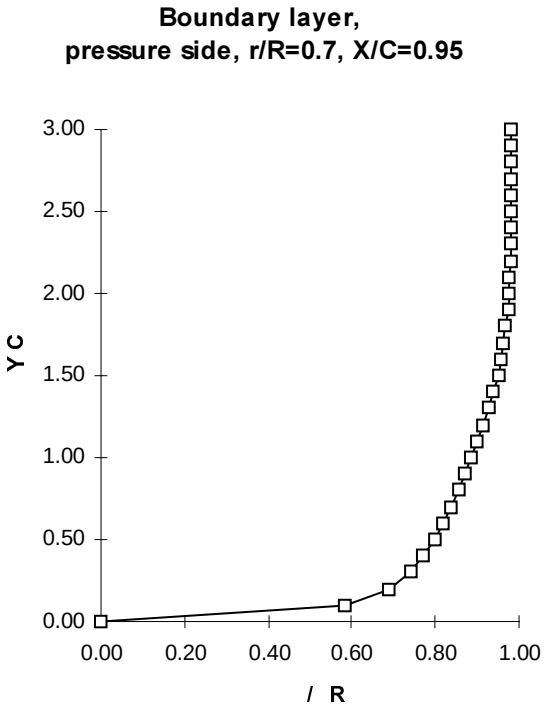

Figure 10. Boundary layer at r/R=0.7 and x/c=0.95 on the blade pressure side.

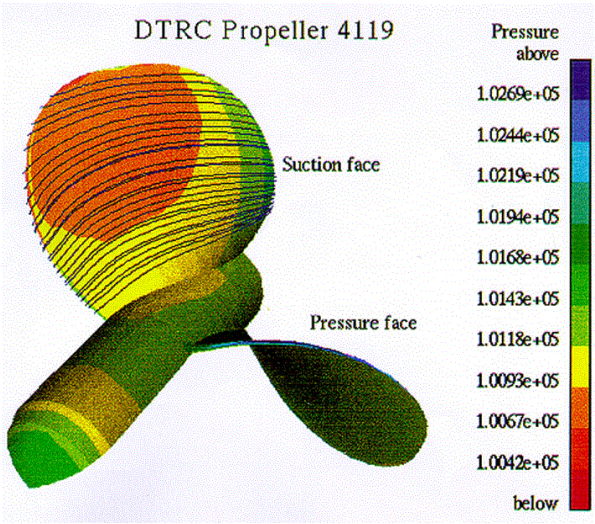

Figure 11. Streamlines and static pressure contours on the blade suction side (J=0.833).

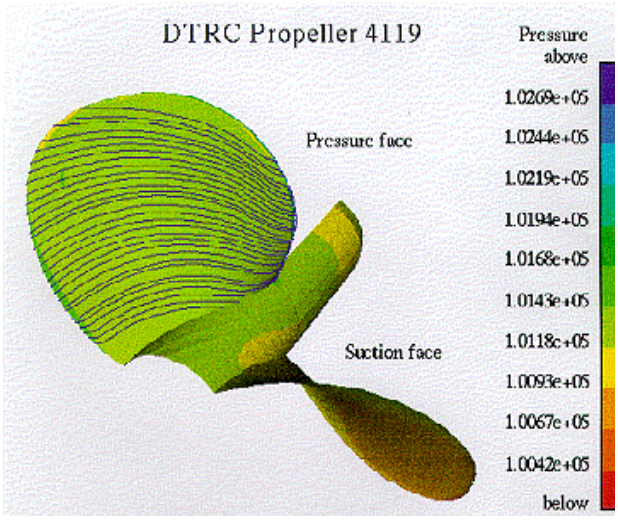

Figure 12. Streamlines and static pressure contours on the blade pressure side (J=0.833).

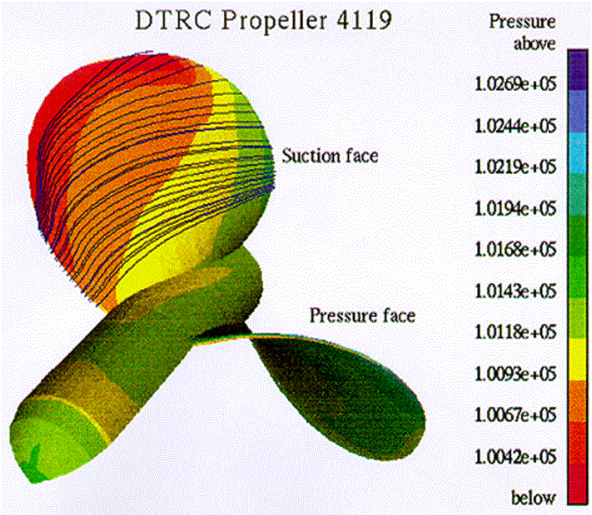

Figure 13. Streamlines and static pressure contours on the blade suction side (J=0.5).

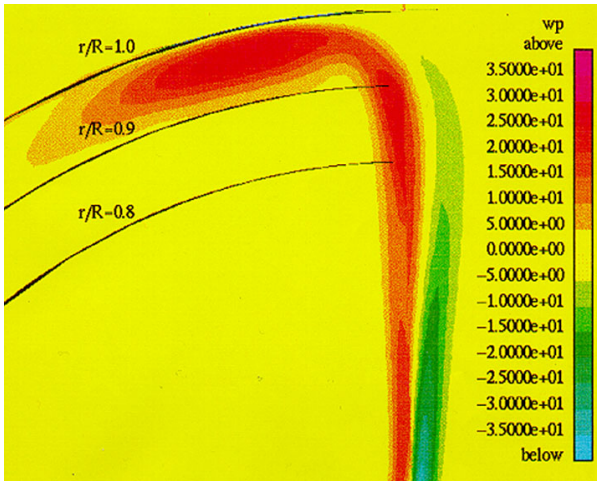

Figure 14. Pitch-line vorticity contours at x/R=0.3281 (J=0.833).